Orbital pathways for Mn^{2+}-carrier sp-d exchange in diluted magnetic semiconductor quantum dots

Rémi Beaulac, Yong Feng, Joseph W. May, Ekaterina Badaeva, Daniel R. Gamelin, and Xiaosong Li

Phys. Rev. B **84**, 195324 — Published 28 November 2011

DOI: 10.1103/PhysRevB.84.195324

October 17, 2011

Orbital pathways for Mn^{2+}-carrier *sp-d* exchange in diluted magnetic semiconductor quantum dots

Rémi Beaulac, Yong Feng, Joseph W. May, Ekaterina Badaeva,

Daniel R. Gamelin,*, [i] and Xiaosong Li*, [ii]

Department of Chemistry, University of Washington, Seattle, WA 98195-1700

Abstract. Manganese-carrier magnetic exchange interactions in strongly quantum confined Mn^{2+}-doped CdSe quantum dots (QDs) having d_{QD} = 1.52, 2.08, and 2.54 nm have been investigated using a combination of density functional theory (DFT) and perturbation theory calculations. Established perturbation expressions have been tested by comparing the exchange energies predicted from these expressions (using DFT results as input parameters) with those calculated directly by DFT. These comparisons allow the dominant orbital pathways responsible for Mn^{2+}-carrier exchange to be identified and analyzed. The Mn^{2+}-valence-band-hole exchange interaction is described well using the long-accepted antiferromagnetic *p-d* kinetic exchange pathway. The Mn^{2+}-conduction-band-electron interaction is described well using the recently proposed ferromagnetic kinetic *s-s* exchange pathway. Antiferromagnetic kinetic *s-d* exchange interactions previously proposed to become dominant in quantum confined diluted magnetic semiconductors (DMSs) have been evaluated quantitatively by both DFT and perturbation theory and are found to be weak compared to the ferromagnetic *s-s* interaction, even in these strongly confined QDs. The magnitudes of the mean-field exchange parameters are found to be nearly independent of quantum confinement over this range of QD diameters, and the dominant orbital pathways are not fundamentally altered by quantum confinement.

i. Gamelin@chem.washington.edu

ii. xsli@uw.edu

PACS numbers: 75.75.LF, 81.05.Dz, 81.07.Ta, 61.72.uj

I. Introduction

In diluted magnetic semiconductors (DMSs), exchange interactions between localized magnetic impurities and delocalized charge carriers give rise to various technologically important effects including giant spin splittings of the semiconductor band structure,[1-3] exciton spin polarization,[4-7] spin-polarized electrical currents,[8,9] excitonic magnetic polarons,[10-16] and carrier-controlled magnetism.[17-20] Within the past decade, attention has turned to magnetically doped semiconductor nanostructures like colloidal or self-assembled DMS quantum dots (QDs),[10,21-23] motivated in part by potential quantum optics or information processing technologies.[24-26] DMSs quantum dots may enable versatile control of magnetism by means unavailable in their bulk counterparts, for example through lattice deformations (piezomagnetism),[27] exchange interactions involving closed-shell QD configurations,[28] and optical or electrical gating.[29-31]

All of the potential spin-electronic and spin-photonic applications of DMSs are ultimately determined by their microscopic dopant-carrier (*sp-d*) magnetic exchange interactions. Most analyses of dopant-carrier magnetic exchange in quantum-confined DMSs have relied on methods developed to describe the corresponding bulk materials.[1-3,32-36] Whereas the general features of *sp-d* exchange appear to translate across length scales, specific contrasts have been emphasized in some cases.[12,13,36-40] Most prominently, a strong quantum-confinement-induced change in the fundamental nature of the conduction-band-electron (e^-_{CB}) – Mn^{2+} exchange (*s-d* exchange) interaction has been described both theoretically[36,37] and experimentally.[37,41-45] According to **k·p**-model descriptions of Mn^{2+}- e^-_{CB} exchange, weak potential *s-d* exchange is the only coupling mechanism in bulk II-VI DMSs because kinetic *s-d* exchange is forbidden by symmetry at $k = 0$, but quantum confinement relaxes this symmetry constraint and allows mixing of valence-band character with *p*-like symmetry into the Bloch functions of the conduction band at finite *k* vectors.[36,37] This mixing has been proposed to turn on strong antiferromagnetic kinetic *s-d* exchange coupling that dominates over the weaker ferromagnetic potential *s-d* exchange coupling in DMS QDs and quantum wells (QWs).[36,37] The existence of strong kinetic *s-d* exchange in DMS QDs and QWs is not universally accepted, however. Tight binding calculations, which also show the appearance of kinetic *s-d* exchange with quantum confinement and inversion of the sign of this exchange interaction at large *k*, predict a smaller dependence on wavevector than derived from the **k·p** model because of smaller predicted *s-d* hybridization.[46]

Recent experimental[47] and theoretical[48] results for II-VI DMSs further challenge the notion that kinetic *s-d* exchange could ever become dominant in Mn^{2+}-based DMSs by drawing attention to the fact that the ferromagnetic *s-d* exchange interaction also strengthens with quantum confinement, counterbalancing any increase in kinetic *s-d* exchange.[48]

Here, we describe the results of density functional theory (DFT) calculations designed to probe dopant-carrier exchange interactions in $Cd_{1-x}Mn_xSe$ QDs in the strong confinement regime. DFT calculations have been applied successfully in recent years to investigate the electronic structure of DMS nanostructures.[31,49-55] In contrast with the highly successful mean-field and virtual-crystal approximations (MFA and VCA) generally applied to interpret experimental data,[1-3] the DFT calculations are atomistic and are therefore not subject to the constraints of ensemble averaging, averaging over dopant positioning within the nanocrystals, or analyses based on effective Hamiltonians. We show that these DFT results can be related to the extensive existing body of experimental literature that does employ the MFA and VCA by collective analysis of exchange energies calculated for the various possible dopant sites within the QDs, illustrating the relationship between atomistic and mean-field exchange energies. The microscopic origins of the *s-d* and *p-d* exchange energies are then examined in detail. The well-known $Mn^{2+}(3d)$-based *p-d* exchange pathway is confirmed to dominate Mn^{2+}-h^{+}_{VB} exchange coupling, and a $Mn^{2+}(4s)$-based *s-s* orbital pathway is found to dominate Mn^{2+}-e^{-}_{CB} exchange coupling at all DMS length scales. The DFT results do not show the dominant kinetic *s-d* exchange postulated to arise in the strong confinement limit,[36,37] suggesting that kinetic *s-d* exchange effects in quantum confined DMSs are not as substantial as previously thought.

II. Methods

Quasi-spherical $Cd_{n-m}Mn_mSe_n$ QDs (where n = 33, 84, and 153 and m = 1, 2, 3) were constructed using the bulk CdSe wurtzite crystal structure with lattice parameters a = 4.2985 Å and c = 7.0152 Å.[56] Each QD has C_{3v} symmetry in the absence of Mn^{2+}. The effective diameters (d_{QD}) of these three QDs are approximately 1.52, 2.08, and 2.54 nm, respectively. These diameters are similar to those of the smallest CdSe QDs obtainable from hot-injection syntheses[57-59] and represent CdSe in the strong quantum confinement regime (CdSe exciton Bohr radius a_0 = 5.6 nm).[60] Pseudo-hydrogen atoms with nuclear charges of +1.5 and +0.5 were used to passivate uncompensated surface Cd^{2+} and Se^{2-} ions (dangling bonds) by formation of fully optimized Cd-H and Se-H bonds, according to the scheme described in recent literature.[49,61,62] This pseudo-hydrogen capping leads to a well-defined bandgap and stable QD geometry. Substitution of Mn^{2+} dopants for the Cd^{2+} ions retains the overall neutral charge of the QDs. DFT calculations were performed with the development version of the Gaussian program.[63] Ground-state energies and electronic structures were obtained by solving the Kohn-Sham equations self-consistently using the PBE1PBE hybrid functional[64-66] with the LanL2DZ basis set,[67-69] in which core electrons are replaced by an effective core potential, and only Cd^{2+} (4*d*, 5*s*, 5*p*), Se^{2-} (4*s*, 4*p*), Mn^{2+} (3*s*, 3*p*, 4*s*, 3*d*) and H (1*s*) electrons are described with explicit basis functions. This computational scheme has been successful in describing the electronic structures of doped ZnO QDs ($Zn_{1-x}TM_xO$, where TM = Co^{2+}, Mn^{2+}).[49,50] We note that spin-orbit coupling is not treated herein, and any effect arising purely from spin-orbit interactions is thus neglected. In CdSe, the spin-orbit splitting of the valence band is larger than the magnetic interactions modeled here ($\Delta E_{SO} \sim 0.4$ eV). Because of this large spin-orbit splitting, the orbital angular momentum of the valence band is quenched and the spin splittings become anisotropic. Other sources of orbital angular momentum quenching (hexagonal lattice, magnetic impurity located away from the crystallite centers, etc.) suggest that the neglect of spin-orbit coupling would not lead to serious error aside from the inability to properly model the anisotropy of this exchange constant.

III. Results of DFT calculations

A. $Cd_{1-x}Mn_xSe$ QD density of states. Figure 1 shows the density-of-states (DOS) diagram calculated for a $Cd_{83}MnSe_{84}$ QD ($d_{QD} \sim 2.08$ nm), with the spin-up (majority) and spin-down (minority) spin densities plotted as positive and negative values, respectively. This DOS diagram shows a filled valence band (VB) and an empty conduction band (CB) separated by a gap with energy $E_g \sim 4.3$ eV. The calculated bandgap changes to 4.8 eV for $Cd_{32}MnSe_{33}$ and to 3.8 eV for $Cd_{152}MnSe_{153}$ QDs,[70] reflecting quantum confinement.[71] These gaps are approximately 70% larger than the optical bandgaps measured for similarly sized CdSe QDs.[58,72] About half of this discrepancy can be ascribed to the exciton binding energy, which is important in optical studies but is not represented in the calculation of DOS diagrams (experimentally worth ~0.6 to 0.9 eV for the QD sizes studied here).[73] The calculated gaps can be improved with the linear response time-dependent DFT (TDDFT)[74] or GW[75] methods, but the computational cost of these methods is impractical for the large systems studied here.

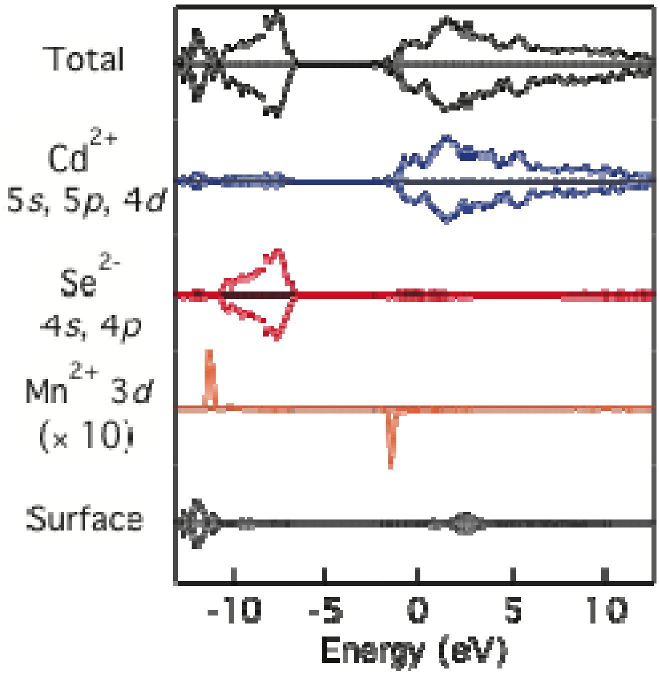

Figure 1. Density-of-states (DOS) diagram calculated for a $Cd_{83}MnSe_{84}$ QD with the Mn^{2+} ion placed at the cation site closest to the QD center. The total DOS is decomposed into its different components (note the 10× magnification of the Mn^{2+} 3*d* component). Spin up: positive density values. Spin down: negative density values. The vertical lines indicate the energy position of the valence band and of the conduction band. A zoomed-in view of the conduction band levels is provided in Fig. 7.

Decomposition of the total densities of Fig. 1 into individual atomic orbital contributions shows that the VB is mostly built out of Se^{2-} 4*p* orbitals, whereas the CB consists predominantly of a mixture of Cd^{2+} 5*s* and 5*p* orbitals. Analysis shows that 78% of the total VB density is located on selenides, a result that agrees well with the ionicity of bulk CdSe (f_i = 78%) determined from Mn^{2+} hyperfine electron paramagnetic resonance (EPR) splittings.[76] The Mn^{2+} 3*d* orbitals are located well outside the gap, with the filled 3*d* levels ~4.5 eV below the top edge of the VB and the empty 3*d* levels ~0.9 eV above the bottom edge of the CB. Experimentally, the filled Mn^{2+} 3*d* orbitals in bulk $Cd_{1-x}Mn_xSe$ have been reported to lie ~3.5 eV below the VB edge,[77-79] in reasonable agreement with the calculations. Both the filled and empty Mn^{2+} 3*d* bands are narrow, indicative of small covalent involvement of these orbitals in the Mn^{2+}-Se^{2-} bonds.[77] Surface states occur well away from the band edges.

B. Electron and hole wavefunctions. To study Mn^{2+}-carrier magnetic exchange interactions, charge carriers need to be introduced. Experimentally, this is most readily done by photoexcitation to generate both electrons and holes, although single charge carriers can also be introduced by electrical or chemical methods.[31,80-82] Here, dopant-carrier exchange interactions in the CdSe QDs are studied by adding or removing one electron, followed by a full electronic wavefunction optimization.

The charge carrier orbitals calculated for a representative $Cd_{83}MnSe_{84}$ QD are presented in Fig. 2. Both carriers delocalize throughout the QD, with atomic contributions reflecting the orbital composition of the wavefunctions at each band edge as described by the DOS diagram of Fig. 1. Fig. 2(c),(d) shows that the e^-_{CB} resides in an orbital primarily composed of Cd^{2+} 5*s* atomic orbitals, and Fig. 2(e),(f) shows that the h^+_{VB} resides in an orbital primarily composed of Se^{2-} 4*p* orbitals. The anisotropy of the hole wavefunction evident in Fig. 2(e) reflects the break in degeneracy of the hole wavefunctions that arises from loss of the C_3 rotational symmetry element of the parent undoped CdSe QD upon introduction of Mn^{2+}. The two carrier densities are also slightly displaced along the C_3 axis, attributable to the polarity of the wurtzite lattice structure and the resulting large ground-state permanent electric dipole moments.[83,84]

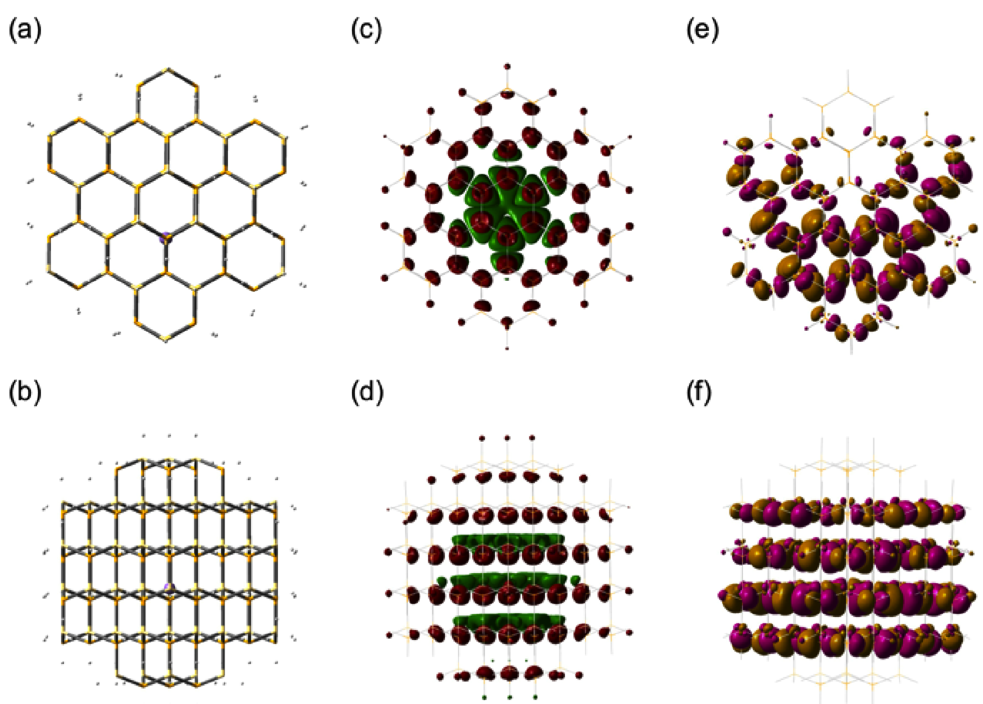

Figure 2. Structure of a wurtzite $Cd_{83}MnSe_{84}$ QD, with the C_3-axis of the parent crystal oriented **(a)** out of the page and **(b)** vertically in the plane of the page. The Mn^{2+} position is indicated with a purple sphere. **(c)** and **(d)**: Electronic wavefunction of an added electron (e^-_{CB}). **(e)** and **(f)**: Electronic wavefunction of an added hole (h^+_{VB}).

C. Mn^{2+}-e^-_{CB} and Mn^{2+}-h^+_{VB} exchange energies. We now address Mn^{2+}-carrier magnetic exchange. Defining the spin-up configuration of the Mn^{2+} ground state as the reference point for the spin-space coordinates, the exchange coupling between the Mn^{2+} and an unpaired band-like electron is antiferromagnetic (AFM) when that electron has the spin-down orientation, and ferromagnetic (FM) when it has the spin-up orientation (for Mn^{2+}-h^+_{VB} exchange, these spin orientations refer to those of the unpaired VB electron, which are opposite those of the VB hole). For any given dopant position $\mathbf{r}_i$, the energy differences between antiferromagnetic and ferromagnetic configurations that result from the Mn^{2+}-e^-_{CB} and Mn^{2+}-h^+_{VB} exchange interactions, $\Delta E_e(\mathbf{r}_i)$ and $\Delta E_h(\mathbf{r}_i)$ respectively, are calculated as described by eqs 1.

$$\Delta E_e(\mathbf{r}_i) = E_e^{AFM}(\mathbf{r}_i) - E_e^{FM}(\mathbf{r}_i) \tag{1a}$$

$$\Delta E_h(\mathbf{r}_i) = E_h^{AFM}(\mathbf{r}_i) - E_h^{FM}(\mathbf{r}_i) \tag{1b}$$

Under this convention, positive energy splittings correspond to net ferromagnetic interactions and negative splittings to net antiferromagnetic interactions.

In the C_{3v} point group symmetry of the parent $Cd_{84}Se_{84}$ crystal, there are ten unique internal cation positions and eleven unique cation positions at the QD surfaces (defined as having at least one cation-H bond). Electronic wavefunction optimization with an added hole or electron was performed for Mn^{2+} at each unique cation position in the $Cd_{83}MnSe_{84}$ QD, and $\Delta E_e(\mathbf{r}_i)$ and $\Delta E_h(\mathbf{r}_i)$ were then calculated. These data can be plotted against a radial coordinate (r),

$$r_i = \left|\mathbf{r}_i - \mathbf{R}_0\right| \tag{2}$$

where $\mathbf{R}_0$ defines the QD center of mass and i indexes the cation positions. Figure 3 plots $\Delta E_e(r_i)$ and $\Delta E_h(r_i)$ values calculated for the various Mn^{2+} positions of the $Cd_{83}MnSe_{84}$ QD, and Table 1 summarizes these values for each unique cation position.

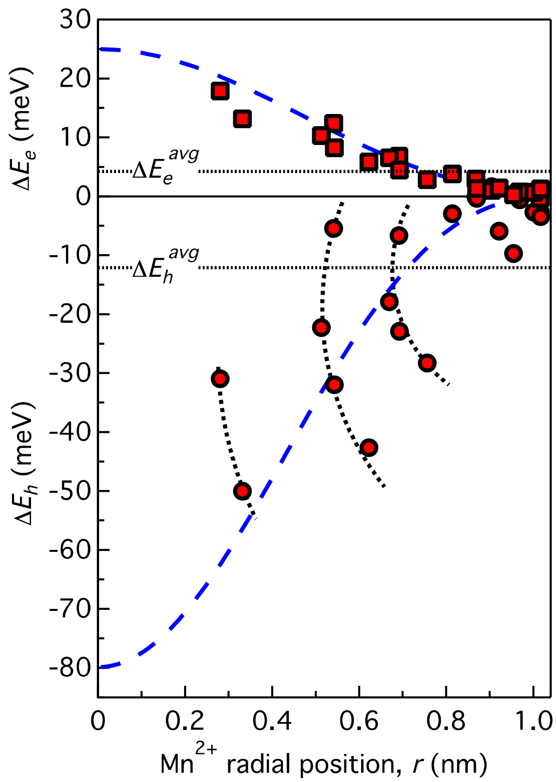

Figure 3. ΔE_e (squares) and ΔE_h (circles) plotted as a function of distance between the Mn^{2+} and the QD center. The dashed lines show the trends expected from a particle-in-a-spherical-well model, eq 7, with a = 1.04 nm, n = 84, N_0 = 17.8 nm^{-3}, ΔE_e^{avg} = 4.2 meV, ΔE_h^{avg} = −12.1 meV. The dotted horizontal lines show the position of the average energy splittings, ΔE_e^{avg} and ΔE_h^{avg}. The dotted black curves are guides to the eye.

The data in Table 1 yield site-probability-weighted average energy splittings of ΔE_e^{avg} = 4.2 meV and ΔE_h^{avg} = −12.1 meV. These average values are close to the smallest calculated energy splittings, reflecting the very high surface-to-volume (S/V) ratios of such small QDs (S/V ~ 3 for $Cd_{83}MnSe_{84}$), *i.e.*, most cations are close to the QD surface, where the energy splitting approaches zero.

Table 1. Energy splittings resulting from addition of one electron or hole to a $Cd_{83}MnSe_{84}$ QD, computed for each unique cation substitution site.

Position index, i	P_i^a	r_i (nm)	ΔE_e (meV)^b	ΔE_h (meV)^b
1	1/28	0.69	6.8	−6.7
2	1/28	0.54	12.4	−5.4
3	1/14	0.67	6.6	−17.9
4	1/28	0.51	10.3	−22.3
5	1/28	0.28	17.9	−31.0
6	1/14	0.69	4.5	−22.9
7	1/28	0.54	8.2	−32.0
8	1/28	0.33	13.1	−50.0
9	1/28	0.76	2.8	−28.3
10	1/28	0.62	5.8	−42.6
11, Surface^c	4/7	–	1.2	−2.5
	Average, ΔE^{avg} $^{d.}$		4.2	−12.1

$^{a.}$ P is the statistical weight, which is calculated via p/n, where n is the total number of cations in the QD and p is the cation site degeneracy arising from the C_{3v} symmetry of the parent *w*-CdSe QD.
$^{b.}$ ΔE_e and ΔE_h are computed using eqs 1a and 1b, respectively.
$^{c.}$ Average values.
$^{d.}$ $\Delta E_{e(h)}^{avg} = \sum_i P_i \cdot \Delta E(r_i)$

D. Mean-field exchange energies from DFT. In the perturbative limit, dopant-carrier magnetic exchange can be described using a simple Heisenberg-Dirac-Van Vleck (HDVV) spin-Hamiltonian (eq 3), where $\hat{S}_i$ and $\hat{\sigma}$ are the spin operators for the dopant ion (located at $\mathbf{r}_i$) and for the charge carrier (located at $\mathbf{r}$), respectively, and $J(\mathbf{r}_i - \mathbf{r})$ is the distance-dependent exchange coupling constant.[1-3]

$$\hat{H}_{HDVV} = \sum -2J(\mathbf{r}_i - \mathbf{r})\hat{S}_i \cdot \hat{\sigma} \tag{3}$$

Experimentally, magnetic exchange energies in DMS QDs are frequently obtained from ensemble averages over dopant positions and distributions of QD shapes and sizes.[1,2,22,85] Such data are best analyzed within the mean-field and virtual crystal approximations. In the MFA, both spin operators in eq 3 can be replaced by their thermodynamical averages $\langle S_z \rangle$ and σ_z, where the Mn^{2+} magnetization is arbitrarily here assigned the spin-up saturation value of $\langle S_z \rangle = +2.5$,[86] and σ_z = +1/2 or −1/2 for spin-up and spin-down electrons, respectively. Introducing the mean-field exchange constants $N_0\alpha$ and $N_0\beta$ for Mn^{2+}-e_{CB}^- and Mn^{2+}-h_{VB}^+ interactions, respectively, the mean-field analogs of eqs 1 can be written as in eqs 4 and 5, with

m as the number of Mn^{2+} dopants per QD and n the total number of cations (Mn^{2+} plus Cd^{2+}) per QD.

$$N_0\alpha = \frac{n \cdot \Delta E_e^{avg}}{m\langle S_z \rangle} \tag{4}$$

$$N_0\beta = \frac{3n \cdot \Delta E_h^{avg}}{m\langle S_z \rangle} \tag{5}$$

Substituting the average exchange energies given in Table 1 (where m/n = 1/84) into eqs 4 and 5 yields $N_0\alpha = 0.141 \pm 0.003$ eV and $N_0\beta = -1.22 \pm 0.01$ eV. These values agree well in both sign and magnitude with the experimental values of +0.26 eV and −1.24 eV measured for bulk $Cd_{1-x}Mn_xSe$.[87] We note that spin-orbit coupling also influences $N_0\beta$[87-89] but is not accounted for here. Overall, the reasonable agreement between experimental and calculated mean-field exchange energies allows the conclusion that DFT captures the essential features of dopant-carrier magnetic exchange in DMS nanostructures.

E. Mn^{2+} position, concentration, and QD size. The dependence of $\Delta E_{e(h)}$ on r in DMS QDs is commonly rationalized using a simple particle-in-a-spherical-well model.[12,13,38] In this model, the particle's ground-state carrier density distribution is given by the square of a zeroth order spherical Bessel function of the first kind (eq 6), where a is the well radius, equated here with the QD radius.

$$\left|\psi(r)\right|^2 = \frac{\sin^2\left(\frac{\pi r}{a}\right)}{2\pi a r^2} \tag{6}$$

The scaling of ΔE_e (ΔE_h) with the carrier probability density is then described in the simplest approximation by eq 7, where N_0 is the cation density (N_0 = 17.8 nm^{-3} for w-CdSe).[90]

$$\Delta E_{e(h)}(r) = \frac{n \cdot \Delta E_{e(h)}^{avg}}{N} \cdot \left|\psi_{e(h)}(r)\right|^2 \tag{7}$$

The dashed curve in Fig. 3 plots $\left|\psi(r)\right|^2$ for the $Cd_{83}MnSe_{84}$ QD estimated from eq 6 using a = 1.04 nm and ΔE_e^{avg} or ΔE_h^{avg} from Table 1. The agreement between eq 7 and DFT is excellent for ΔE_e, but only the general trend is reproduced for ΔE_h. Instead of a smooth increase in ΔE_h as Mn^{2+} approaches the QD center, the ΔE_h values from DFT show considerable but systematic scatter. This scatter is interpreted as reflecting the anisotropy of the hole wavefunction shown in Figs. 2(c),(d), meaning the spherical potential model is not a good approximation for off-center doping.[91] Several studies have emphasized the role of hole density anisotropy in leading to interesting magnetic effects.[11,15,88,89,92] A detailed analysis of these anisotropic effects is beyond the scope of this study and will be explored further in a future investigation.

For a fixed dopant position near the QD center, ΔE_e and ΔE_h can also be tuned by changing the confinement volume. Figure 4(a) plots $\Delta E_{e(h)}$ as a function of QD diameter for $Cd_{32}MnSe_{33}$ (d_{QD} = 1.52 nm), $Cd_{83}MnSe_{84}$ (d_{QD} = 2.08 nm), and $Cd_{152}MnSe_{153}$ (d_{QD} = 2.54 nm) QDs, with the dopant position chosen to be as near as possible to the center of each QD. As d_{QD} decreases, $\Delta E_{e(h)}$ increases because of increasing carrier density near the QD center. Importantly, the signs of the Mn^{2+}-e^-_{CB} and Mn^{2+}-h^+_{VB} exchange splittings remain the same for all QD sizes. Figure 4(b) shows that ΔE_e^{avg} and ΔE_h^{avg} scale with the inverse $Cd_{n\text{-}1}MnSe_n$ QD volume (given here as $1/n$), which in turn indicates that $N_0\alpha$ and $N_0\beta$ do not change significantly over this QD size range (see eqs 4, 5).

Figure 2 also shows that charge carriers are delocalized throughout the QDs, and hence can be exchange coupled to multiple Mn^{2+} ions simultaneously if the QD contains more than one dopant. This scenario can potentially lead to spontaneous ferromagnetic ordering of the Mn^{2+} spin sub-lattice, as observed experimentally in bound and excitonic magnetic polarons.[10,11,14-16,88,92] To explore this scenario computationally, CdSe QDs doped with two and three Mn^{2+} ions were also investigated. For these calculations, the dopants were positioned at second nearest neighbor sites to avoid the well-known Mn^{2+}-Mn^{2+} antiferromagnetic superexchange interactions, which drop to a negligibly small value at this distance.[2,34,93,94] The positions chosen were the three equivalent sites designated by the index 4 in Table 1 for the $Cd_{84\text{-}m}Mn_mSe_{84}$ QDs, and the same positions for the other two QD sizes. Figure 4(c) plots $\Delta E_{e(h)}$ vs m for the three different QD sizes studied here. Both ΔE_e and ΔE_h increase linearly with m, showing that the Mn^{2+} ions contribute additively to the total exchange splittings. This result justifies application of the MFA for analysis of excitonic Zeeman splittings in excitonic magnetic polarons and magneto-optical measurements performed on DMS QD ensembles.

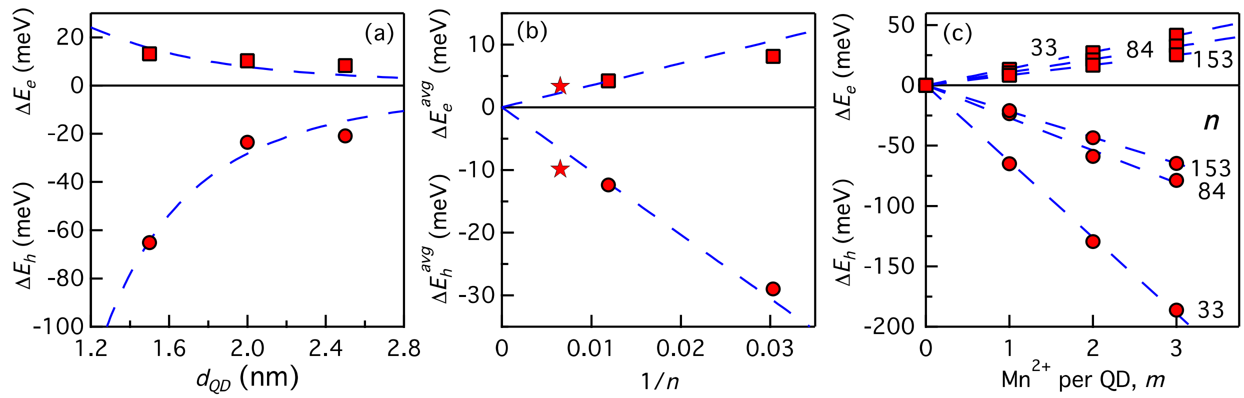

Figure 4. (a) Band-edge energy splittings resulting from addition of an electron (squares) or a hole (circles) to $Cd_{n\text{-}1}MnSe_n$ QDs, plotted vs QD diameter ($Cd_{32}MnSe_{33}$ (d_{QD} = 1.52 nm), $Cd_{83}MnSe_{84}$ (d_{QD} = 2.08 nm), and $Cd_{152}MnSe_{153}$ (d_{QD} = 2.54 nm)). The Mn^{2+} occupies the cation positions closest to the QD centers. The dashed lines are guides to the eye. **(b)** Position-averaged energy splittings of the same QDs plotted vs inverse QD volume (in number of cations unit, n). The dashed lines are from eqs 4 and 5, with m = 1, $\langle S_z \rangle = 2.5$, $N_0\alpha$ = 0.14 eV, and $N_0\beta$ = -1.22 eV. The energies for the biggest dot (red stars) were extrapolated from the data in Fig. 4(a) by assuming the density distribution given by eq 6. The other energies come from averaging over explicit calculations for each Mn^{2+} position. **(c)** Mn^{2+}-carrier exchange splittings (circles: ΔE_h; squares: ΔE_e) plotted vs the number of Mn^{2+} per QD for three $Cd_{n-m}Mn_mSe$ QD sizes (n = 33, 84, and 153), with the Mn^{2+} ions at position 4 (Table 1). The dashed lines are linear fits.

Overall, these results demonstrate the ability of DFT to describe exchange interactions between highly localized Mn^{2+} spins and delocalized charge carriers in semiconductor nanostructures. When analyzed collectively, the DFT results yield mean-field exchange energies that agree well with experimental values for bulk DMSs in both sign and magnitude. When analyzed individually, the DFT calculations show a dependence of the exchange splitting on Mn^{2+} position that maps the carrier probability density distribution within the QDs. We now turn to a more detailed analysis of the DFT results, with emphasis on description of the microscopic orbital pathways responsible for these exchange splittings.

IV. Analysis

A. General aspects of magnetic exchange interactions. The DFT results presented above provide a window into the microscopic origins of dopant-carrier magnetic exchange in DMSs. Following Anderson,[95,96] magnetic exchange interactions can be classified into two distinct groups, potential exchange and kinetic exchange, with energies parameterized by the exchange coupling constants J_{pot} and J_{kin}. Potential exchange (or "direct exchange") refers to the ubiquitous two-electron Coulomb exchange that arises from Pauli's exclusion principle. Given two magnetic orbitals ψ_i and ψ_j, J_{pot} is described by eq 8, where $\mathbf{r}_1$ and $\mathbf{r}_2$ describe the spatial coordinates of each electron.

$$J_{pot} = \left\langle \psi_i(\mathbf{r}_1)\psi_j(\mathbf{r}_2) \middle| (\mathbf{r}_1 - \mathbf{r}_2)^{-1} \middle| \psi_j(\mathbf{r}_1)\psi(\mathbf{r}_2) \right\rangle \tag{8}$$

Potential exchange energies are greatest when ψ_i and ψ_j are either orthogonal orbitals of the same center (intra-atomic exchange) or non-overlapping orbitals of neighboring centers.

Kinetic exchange is a two-center phenomenon involving partial transfer of spin density from one magnetic center onto the other. This transfer is generally treated using perturbation theory, leading to expressions such as eq 9,[97,98] where C_{ij} is an orbital-pathway-dependent constant, h_{ij} is the so-called "transfer-integral" (or "hybridization matrix element", or "hopping integral") that describes mixing between the two orbitals (ψ_i and ψ_j) participating in the transfer, and $\Delta E_{i\to j}$ is the energy associated with complete transfer of an electron from ψ_i into ψ_j. The sum is taken over all relevant orbital pathways but is most strongly influenced by the lowest energy pathways.

$$J_{kin} = \sum C_{ij} \frac{h_{ij}^2}{\Delta E_{i\to j}} \tag{9}$$

When allowed, kinetic exchange usually dominates the overall magnetic exchange interaction. Whereas potential exchange interactions are always ferromagnetic, kinetic exchange interactions can be either antiferromagnetic or ferromagnetic. In the special case of coupling between two half-filled orbitals, kinetic exchange leads to antiferromagnetic spin alignment because transfer can only occur when the two interacting spins are anti-parallel. In other cases, such as transfer of spin density from a half-occupied orbital of center *a* into an empty orbital of center *b*, or from a doubly occupied orbital of *a* into a half-occupied orbital of *b*, kinetic exchange can stabilize the ferromagnetic alignment of *a* and *b* spins.[98] Below, we analyze the DFT results to identify the specific microscopic orbital pathways that make the dominant contributions to the Mn^{2+}-e_{CB}^{-} and Mn^{2+}-h_{VB}^{+} exchange energies reported above.

B. Mn^{2+}-h_{VB}^{+} exchange coupling: *p-d* orbital pathways. Mn^{2+}-h_{VB}^{+} exchange interactions in DMSs were recognized early on as arising from kinetic exchange involving hybridization of the Mn^{2+} 3*d* orbitals with the semiconductor anion *p* orbitals, leading to the name "*p-d* exchange".[1,2,32-35] Two transfer processes contribute (Fig. 5): (1) transfer of a Mn^{2+} $3d(\uparrow)$ electron into the VB, and (2) transfer of a $VB(\downarrow)$ electron into a half-occupied Mn^{2+} 3*d* orbital. The relevant values of $\Delta E_{i\rightarrow j}$ are thus those of the $Mn^{2+/3+}$ (donor) and $Mn^{2+/+}$ (acceptor) transitions involving the VB edge. These energies can be estimated from the energy differences between the filled and empty 3*d* orbitals and the VB edge in Fig. 1, respectively. The exchange energy associated with this *p-d* orbital pathway is then given by eq 10, where $V_{pd}(r)$ is the $Mn^{2+}(3d)$-VB transfer integral.

$$\Delta E_{pd}(\mathbf{r}_i) = -\frac{mV_{pd}^2(\mathbf{r}_i)}{3n}\left(\frac{1}{E_{3d\downarrow}-E_{VB}}+\frac{1}{E_{VB}-E_{3d\uparrow}}\right) \tag{10}$$

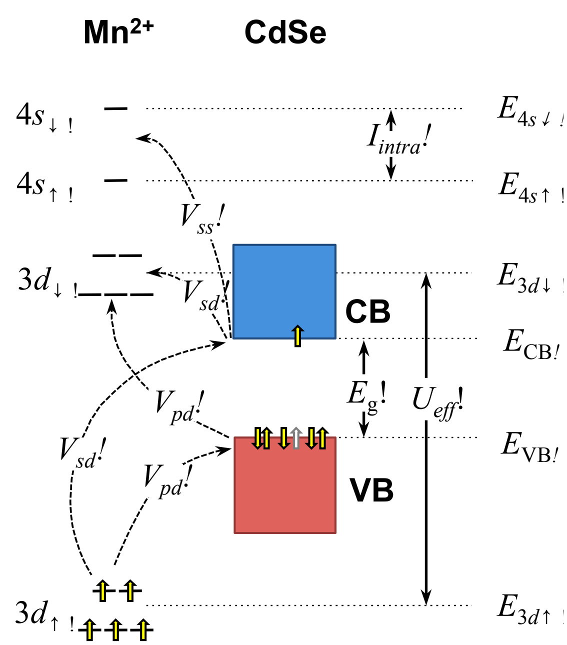

Figure 5. Energy levels involved in Mn^{2+}-carrier magnetic exchange in $Cd_{1-x}Mn_xSe$ DMSs. The alignment of the Mn^{2+} orbitals relative to the CdSe band edges is drawn to be consistent with the DOS obtained from DFT (Fig. 1), although this ordering is not known well from experiment. The Mn^{2+} 4*s* orbital may lie below the empty 3*d* orbitals.[99-101]

The importance of this *p-d* orbital pathway can be evaluated quantitatively by analysis of 3*d*-VB hybridization. Using first-order perturbation theory, the Mn^{2+} 3*d* contribution to the VB-edge wavefunction probability density (f_{3d}^{h}) can be described by eq 11a. Equation 11b is obtained from substitution of eq 10 into eq 11a. Importantly, perturbation theory thus predicts a linear relationship between ΔE_{pd} and f_{3d}^{h}.

$$f_{3d}^{h}(\mathbf{r}_i)=\left|\left\langle \psi_{3d}(\mathbf{r}-\mathbf{r}_i)\middle|\psi_h(\mathbf{r})\right\rangle\right|^2=\frac{mV_{pd}^2(\mathbf{r}_i)}{3n}\left(\frac{1}{E_{3d\downarrow}-E_{VB}}+\frac{1}{E_{VB}-E_{3d\uparrow}}\right)^2 \tag{11a}$$

$$=-\Delta E_{pd}(\mathbf{r}_i)\left(\frac{1}{E_{3d\downarrow}-E_{VB}}+\frac{1}{E_{VB}-E_{3d\uparrow}}\right) \tag{11b}$$

In the limit where Mn^{2+}-h_{VB}^{+} exchange is dominated by the *p-d* orbital pathway, $\Delta E_h \approx \Delta E_{pd}$ and hence proportional to f_{3d}^{h} according to eq 11b. DFT calculations allow evaluation of the relationship between ΔE_h and f_{3d}^{h}. For comparison with eq 11b, f_{3d}^{h} values were calculated from the DFT orbital descriptions of $Cd_{83}MnSe_{84}$ QDs for each unique Mn^{2+} position in Table 1 using the Mulliken approach.[102] ΔE_h values were also calculated for each QD by DFT. Figure 6(a) plots f_{3d}^{h} vs ΔE_h for each unique Mn^{2+} position. As anticipated by eq 11b, there is indeed a linear correlation, with f_{3d}^{h} decreasing to zero as ΔE_h approaches zero. The hole wavefunction contains up to ~2% Mn^{2+} 3*d* character, despite the fact that the Mn^{2+} 3*d* levels are deep within the VB.

For quantitative comparison, the dashed blue line in Fig. 6(a) plots the relationship between ΔE_h and f_{3d}^{h} predicted by perturbation theory for the $Cd_{83}MnSe_{84}$ QDs under the assumption that $\Delta E_h \approx \Delta E_{pd}$, calculated from eq 11b using input parameters taken from the DFT DOS results (Table 2). A small horizontal offset of +3.3 meV has been included to fit the DFT data points. Whereas eq 11 assumes a specific orbital exchange pathway, the DFT calculations make no such assumption and include all possible orbital pathways. The overall excellent agreement between DFT and perturbation theory therefore validates the established description of Mn^{2+}-f_{3d}^{h} magnetic exchange coupling as dominated by a kinetic *p-d* orbital exchange pathway (*i.e.,* $\Delta E_h \cong \Delta E_{pd}$).[34] Although the positive *x* intercept is probably not significant within the precision of the Mulliken analysis used to determine f_{3d}^{h}, it may possibly reflect other weak ferromagnetic kinetic exchange interactions involving higher-energy empty Mn^{2+} orbitals (for instance, the empty Mn^{2+} 4*p* orbitals possess the correct symmetry to hybridize with the VB edge). Finally, from eq 10, $\Delta E_h^{avg} = -12.1$ meV (Table 1), and the Mn^{2+} 3*d* orbital energies listed in Table 2, the average *p*-*d* transfer integral is $\left|V_{pd}^{avg}\right| = 2.72$ eV.

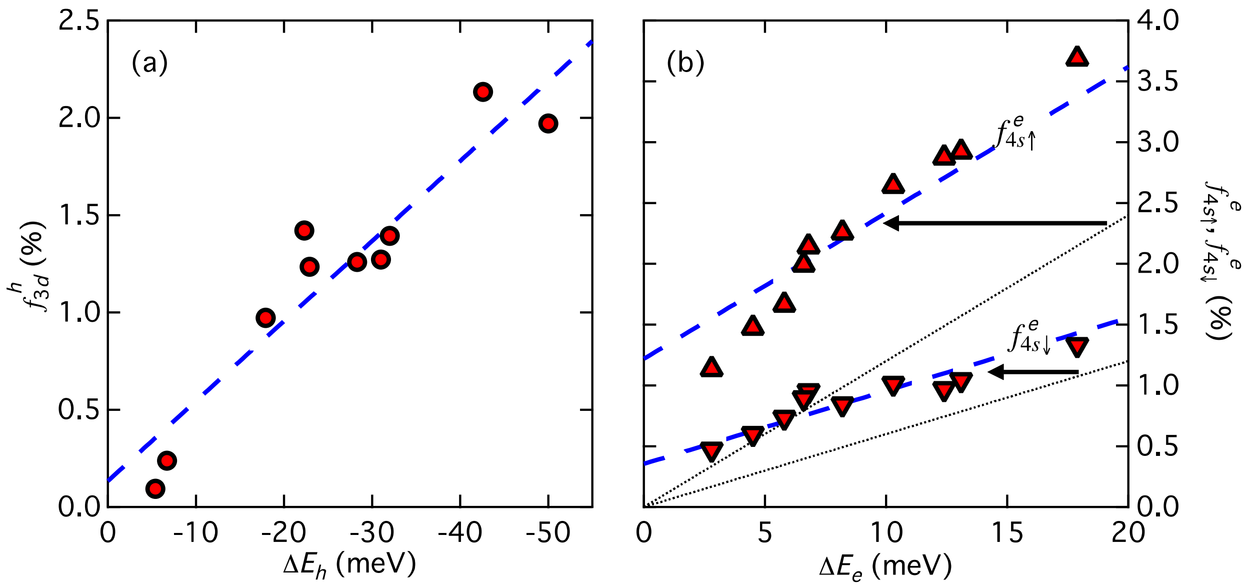

Figure 6. (a) The Mn^{2+} 3*d* contribution to the VB-edge wavefunction probability density (f_{3d}^h) plotted vs the Mn^{2+}-h_{VB}^+ exchange splitting for a $Cd_{83}MnSe_{84}$ QD. The circles come from values of f_{3d}^h and ΔE_h calculated by DFT *via* brute force. The dashed line shows the relationship calculated from perturbation theory (eq 11b) using input parameters from DFT (Table 2) and assuming $\Delta E_{pd} = \Delta E_h$. The slope of the dashed line is -0.04 %$\cdot$meV^{-1} and its *x* intercept is 3.3 meV. Surface positions are not included in this figure. **(b)** Fractional Mn^{2+} 4*s* density in the CB-edge wavefunction probability density ($f_{4s\uparrow}^e$ and $f_{4s\downarrow}^e$) plotted vs the Mn^{2+}-e_{CB}^- exchange splitting for a $Cd_{83}MnSe_{84}$ QD, obtained from DFT. The dotted lines show the relationships obtained from perturbation theory (eq 14) using DFT input parameters (Table 2) and assuming $\Delta E_{ss} = \Delta E_e$. Their slopes are 0.12 %$\cdot$meV^{-1} ($f_{4s\uparrow}^e$) and 0.06 %$\cdot$meV^{-1} ($f_{4s\downarrow}^e$). The dashed lines have the same slopes but are offset with *x* intercept values of -10.2 meV ($f_{4s\uparrow}^e$) and -5.9 meV ($f_{4s\downarrow}^e$), as indicated by the horizontal arrows. Surface positions are not included in this figure.

Table 2. Parameters extracted from DFT results for $Cd_{83}MnSe_{84}$ QDs.

$E_{3d\downarrow} - E_{VB}$	5.3 eV	$E_{4s\uparrow} - E_{CB}$	3.1 eV	$E_{3d\downarrow} - E_{CB}$	0.9 eV
$E_{VB} - E_{3d\uparrow}$	4.5 eV	$E_{4s\downarrow} - E_{CB}$	4.3 eV	$E_{CB} - E_{3d\uparrow}$	8.9 eV
U_{eff}	9.8 eV	I_{intra}	1.2 eV	E_g	4.3 eV
ΔE_{pd}^{avg}	−12.1 meV	ΔE_{ss}^{avg}	6.7 meV	ΔE_{sd}^{avg}	−2.5 meV
$\left\|V_{pd}^{avg}\right\|$	2.72 eV	$\left\|V_{ss}^{avg}\right\|$	2.74 eV	$\left\|V_{sd}^{avg}\right\|$	0.41 eV
$N_0\beta$	−1.22 eV	$N_0\alpha$	0.141 eV		

C. Mn^{2+}-e_{CB}^{-} exchange coupling. We now examine the microscopic origins of Mn^{2+}-e_{CB}^{-} exchange. As introduced above, the ferromagnetic Mn^{2+}-e_{CB}^{-} coupling observed in bulk DMSs is generally described as arising from potential exchange between *k*-like CB electrons and Mn^{2+} *d* electrons.[1,2] It was recently proposed that this interaction could alternatively be described in an explicit two-center formulation as a ferromagnetic kinetic *s*-*s* exchange process involving partial spin transfer from the CB to the empty Mn^{2+} 4*s* orbital.[48] Although the traditional *k*-vector description of "potential" *s*-*d* exchange in bulk DMSs implicitly assumes this interaction, the two-center description allows Mn^{2+}-e_{CB}^{-} exchange to be parameterized explicitly using the same perturbation approach that is already so successfully used to describe Mn^{2+}-h_{VB}^{+} *p*-*d* exchange (*vide supra*).

In quantum confined DMSs, a second kinetic exchange process is widely believed to become important.[36,37,41-45] Although formally forbidden by symmetry in the bulk limit, Mn^{2+} 3*d* hybridization with the CB-edge wavefunction is allowed in quantum confined DMSs and has been predicted to yield strong antiferromagnetic kinetic *s*-*d* exchange coupling in the strong confinement regime.[36,37] Assuming no other orbital pathways are involved, the overall Mn^{2+}-e_{CB}^{-} exchange splitting ΔE_e can thus be written as the sum of these two competing contributions as shown in eq 12, with the sign of ΔE_e ultimately determined by the relative magnitudes of ΔE_{ss} and ΔE_{sd}.

$$\Delta E_e = \Delta E_{ss} + \Delta E_{sd} \tag{12}$$

The DFT results presented here allow ΔE_{ss} and ΔE_{sd} to be determined individually, providing quantitative assessments of the magnitudes of each in strongly confined DMSs, independent of the assumptions of the **k·p** or tight-binding electronic-structure models and also independent of any models of magnetic-exchange coupling. The results of these DFT calculations are compared with those of perturbation theory.

***(i) s-s* orbital pathway.** Figure 7 plots the CB portion of the DOS diagram from Fig. 1 on an expanded energy scale, along with the fractional contributions of the Mn^{2+} 3*d* and 4*s* orbitals. Sizable hybridization of the Mn^{2+} 4*s* orbital with the CB is evident. The Mn^{2+} 4*s* orbital is distributed over ~8 eV in the CB, with an average energy of ~4 eV above the CB edge. Importantly, Fig. 7 shows that the 4*s*(↑) components are on average ~1.2 eV closer to the CB edge than the 4*s*(↓) components are. This spin splitting arises from ferromagnetic intra-ion exchange coupling with the orthogonal half-filled 3*d* orbitals (I_{intra}), which is the same exchange interaction that leads to the Mn^+ free ion having a ^7S ($3d^54s^1$) ground state.[101] The calculated 4*s*(↑)–4*s*(↓) splitting of 1.2 eV compares well with the experimental $^5S_2$–$^7S_3$ energy splitting of the Mn^+ free ion ($I_{intra}^{free\ ion}$ = 1.2 eV).[101] Electron delocalization from the CB into this spin-split Mn^{2+} 4*s* orbital is the primary microscopic process responsible for $N_0\alpha$ in bulk DMSs.[48]

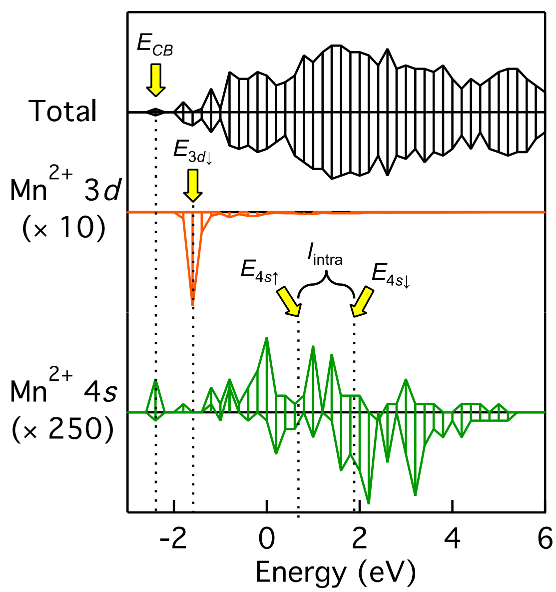

Figure 7. DOS diagram of the CB levels of a $Cd_{83}MnSe_{84}$ QD (Mn^{2+} closest to the QD center), and Mn^{2+} 3*d* and 4*s* contributions (expanded for clarity).

To describe this interaction using perturbation theory, transfer of the e_{CB}^- into the empty Mn^{2+} 4*s*(↑) orbital (ferromagnetic contribution) and into the empty Mn^{2+} 4*s*(↓) orbital (antiferromagnetic contribution) must both be considered. Assuming both transfer integrals are the same (V_{ss}), these interactions yield a net ferromagnetic alignment because of the smaller energy gap separating the CB from the Mn^{2+} 4s(↑) orbital. The energy associated with this kinetic s-s exchange pathway is, in second-order, given by eq 13.[48]

$$\begin{aligned}\Delta E_{ss}(\mathbf{r}_i) &= \frac{m\langle S_z\rangle}{n(S_{Mn}+1/2)}V_{ss}^2(\mathbf{r}_i)\left(\frac{1}{E_{4s\uparrow}-E_{CB}}-\frac{1}{E_{4s\downarrow}-E_{CB}}\right)\\ &= \frac{m\langle S_z\rangle}{n(S_{Mn}+1/2)}V_{ss}^2(\mathbf{r}_i)\frac{I_{intra}}{(E_{4s\uparrow}-E_{CB})(E_{4s\downarrow}-E_{CB})}\end{aligned} \tag{13}$$

Paralleling eq 11, the Mn^{2+} 4s character in the e_{CB}^- density is given by eq 14, which predicts linear relationships between f_{4s}^e and ΔE_{ss} for each spin.

$$\begin{aligned}f_{4s}^e(\mathbf{r}_i) = \left|\langle\psi_{4s\uparrow}(\mathbf{r}_i-\mathbf{r})|\psi_e(\mathbf{r})\rangle\right|^2 &= \frac{m\langle S_z\rangle}{n(S_{Mn}+1/2)}\frac{V_{ss}^2}{(E_{4s\uparrow}-E_{CB})^2}\\ &= \frac{\Delta E_{ss}(\mathbf{r}_i)}{I_{intra}}\frac{E_{4s\downarrow}-E_{CB}}{E_{4s\uparrow}-E_{CB}}\end{aligned} \tag{14a}$$

$$\begin{aligned}f_{4s\downarrow}^e = \left|\langle\psi_{4s\downarrow}(\mathbf{r}-\mathbf{r}_i)|\psi_e(\mathbf{r})\rangle\right|^2 &= \frac{m\langle S_z\rangle}{n(S_{Mn}+1/2)}\frac{V_{ss}^2(\mathbf{r}_i)}{(E_{4s\downarrow}-E_{CB})^2}\\ &= \frac{\Delta E_{ss}(\mathbf{r}_i)}{I_{intra}}\frac{E_{4s\uparrow}-E_{CB}}{E_{4s\downarrow}-E_{CB}}\end{aligned} \tag{14b}$$

Equation 13 predicts ΔE_{ss} to depend on both V_{ss} and the Mn^{2+}(4s)-e_{CB}^- energy spacings. For a given QD, the impact of the Mn^{2+}(4s)-e_{CB}^- energy spacing can be explored by artificially scaling the LANL2DZ core pseudo-potential of the Mn^{2+} ion, which selectively shifts the energy of the Mn^{2+} 4s orbital relative to the CB edge.[70] Figure 8(a) plots ΔE_e for $Cd_{83}MnSe_{84}$ as a function of Mn^{2+} position, calculated for three different Mn^{2+} core pseudo-potentials. The Mn^{2+} 4s energy is tuned by over 270 meV across this series. As anticipated from eq 13, a smaller energy spacing between the CB and the Mn^{2+} 4s orbital increases ΔE_e, and vice versa. Following eq 14, Fig. 8(b) replots these results as $f_{4s\uparrow}^e - f_{4s\downarrow}^e$ vs ΔE_e (with $f_{4s\uparrow}^e$ and $f_{4s\downarrow}^e$ calculated using the Mulliken approach[102] and ΔE_e calculated as in eq 1a), yielding the important conclusion that ΔE_e is linearly correlated with the differential spin density in the Mn^{2+} 4s orbital, largely independent of the actual Mn^{2+} 4s energies. These results provide strong evidence that Mn^{2+}-e_{CB}^- coupling is dominated by the kinetic s-s exchange pathway, even in these strongly quantum confined QDs.[48] From Fig. 8(b), a ~1% difference between spin-up and spin-down e_{CB}^- density in the Mn^{2+} 4s

orbital is ultimately responsible for the observed Mn^{2+}-e^{-}_{CB} exchange energies. Figure 8(b) thus illustrates that a spin-dependent hybridization of band and local wavefunctions is responsible for what is usually referred to as potential *s*-*d* exchange.

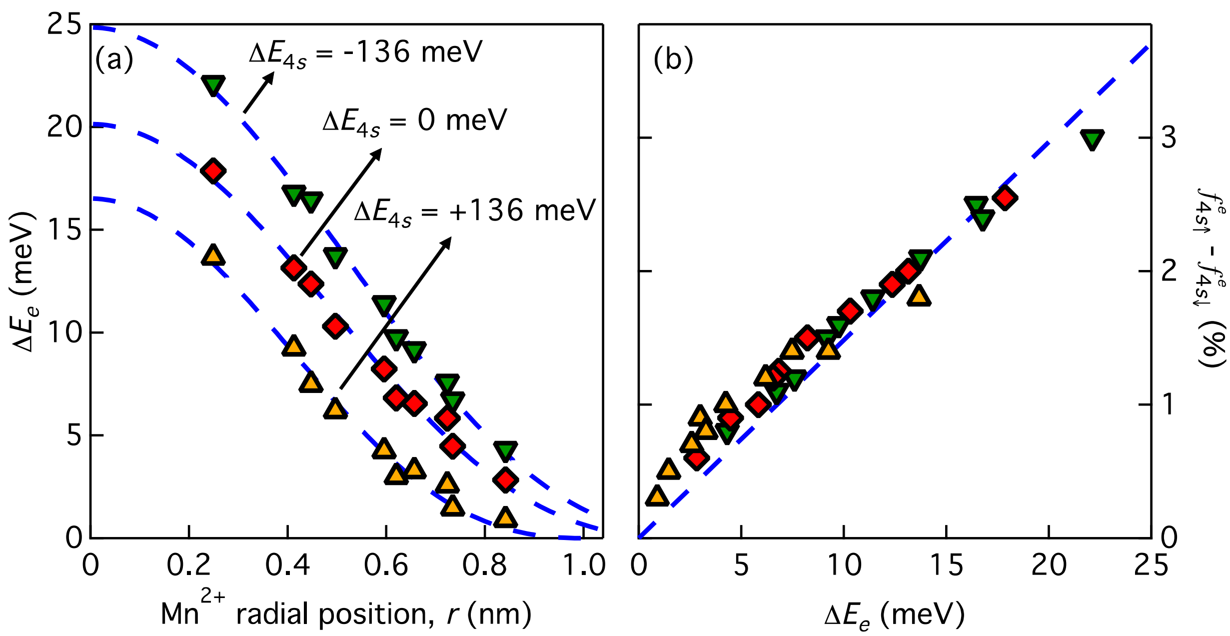

Figure 8. (a) ΔE_e as a function of distance (r) between Mn^{2+} and the center of the $Cd_{83}MnSe_{84}$ QD, for three different Mn^{2+} core pseudo-potentials. The relative shifts in Mn^{2+} 4*s* energy are indicated. The dashed lines are guides to the eye. The surface positions are not included in this figure. **(b)** The data from (a) re-plotted as ΔE_e vs the difference between $f^e_{4s\uparrow}$ and $f^e_{4s\downarrow}$. The dashed line is a global linear fit.

To test eq 14 more directly, $f^e_{4s\uparrow}$ and $f^e_{4s\downarrow}$ from DFT are plotted individually vs ΔE_e in Fig. 6(b). Linear relationships between f^e_{4s} and ΔE_e are indeed observed. $f^e_{4s\uparrow}$ and $f^e_{4s\downarrow}$ were also calculated by the perturbation approach: Substituting the relevant energy parameters from Table 2 into eq 14 yields $f^e_{4s\uparrow}$ and $f^e_{4s\downarrow}$ for each Mn^{2+} position in the $Cd_{83}MnSe_{84}$ QD, and the relationships between these parameters and ΔE_e are plotted as dotted lines in Fig. 6(b). The slopes of these dotted lines agree well with those from DFT, confirming that the *s*-*s* interaction makes the primary contribution to Mn^{2+}-e^{-}_{CB} exchange coupling. Unlike the perturbation result, however, ΔE_e from DFT does not go to zero when $f^e_{4s\uparrow}$ and $f^e_{4s\downarrow}$ equal zero, suggesting that ΔE_e cannot be associated exclusively with ΔE_{ss}. Another orbital pathway must be considered.

Allowing the x intercept to float yields offsets of ~−5 to −10 meV. As described below and by eq 12, this negative x intercept comes from kinetic s-d exchange coupling.

(*ii*) *s-d* orbital pathways. Kinetic s-d exchange is formally analogous to the kinetic p-d exchange described above, with the CB electron wavefunction replacing that of the VB hole. It can be described using the perturbation expression shown in eq 15.

$$\Delta E_{sd}(\mathbf{r}_i) = -\frac{m}{n} V_{sd}^2(\mathbf{r}_i)\left(\frac{1}{E_{3d\downarrow} - E_{CB}} + \frac{1}{E_{CB} - E_{3d\uparrow}}\right) \tag{15}$$

Following the same approach used in the preceding sections, the fraction of Mn^{2+} 3d character in the e_{CB}^- density is given by eq 16, which predicts a linear relationship between f_{3d}^e and ΔE_{sd}.

$$\begin{aligned} f_{3d}^e(\mathbf{r}_i) = \left|\langle \psi_{3d}(\mathbf{r}-\mathbf{r}_i) | \psi_e(\mathbf{r})\rangle\right|^2 &= \frac{m}{n} V_{sd}^2(\mathbf{r}_i)\left(\frac{1}{E_{3d\downarrow} - E_{CB}} + \frac{1}{E_{CB} - E_{3d\uparrow}}\right)^2 \\ &= -\Delta E_{sd}(\mathbf{r}_i)\left(\frac{1}{E_{3d\downarrow} - E_{CB}} + \frac{1}{E_{CB} - E_{3d\uparrow}}\right) \end{aligned} \tag{16}$$

Equation 16 thus allows the contribution of ΔE_{sd} to ΔE_e in eq 12 to be evaluated quantitatively. To test this relationship by DFT, f_{3d}^e values were calculated for the various Mn^{2+} positions in both $Cd_{83}MnSe_{84}$ and $Cd_{32}MnSe_{33}$ QDs using the Mulliken approach[102] and the results are plotted in Fig. 9(a) vs ΔE_e, which was calculated as in eq 1a. From these results, the e_{CB}^- wavefunction density in the $Cd_{83}MnSe_{84}$ QDs has ~0.3% Mn^{2+} 3d character, roughly independent of the Mn^{2+} position. Using eq 16 and energies from Table 2, this hybridization corresponds to $\Delta E_{sd} = -2.5$ meV, again roughly independent of Mn^{2+} position. From Fig. 9(a), we conclude that f_{3d}^e is largely independent of ΔE_e in these QDs, indicating that kinetic s-d exchange does not determine Mn^{2+}-e_{CB}^- magnetic exchange coupling in strongly quantum confined $Cd_{1-x}Mn_xSe$ QDs.

With these results, ΔE_e in this QD can be fully characterized. Figure 9(b) re-plots $f_{4s\uparrow}^e$ and $f_{4s\downarrow}^e$ vs ΔE_e from Fig. 6(b). The dashed lines now represent ΔE_e as the sum of ΔE_{ss} (Fig 6(b)) and ΔE_{sd} (= −2.5 meV, position independent) predicted by perturbation theory. The difference between the DFT results and the perturbation theory predictions is relatively small and systematic, and can be attributed in large measure to the challenge of accurately estimating the relevant excited-state energies needed for the perturbation calculations from the output of the

DFT calculations. We conclude that the perturbation description successfully captures the essence of the Mn^{2+}- e^{-}_{CB} magnetic exchange coupling, and even reproduces the DFT results to a reasonable quantitative extent. Excellent quantitative reproduction of the DFT results can be achieved with only small changes to the 4*s* energies used above.[70]

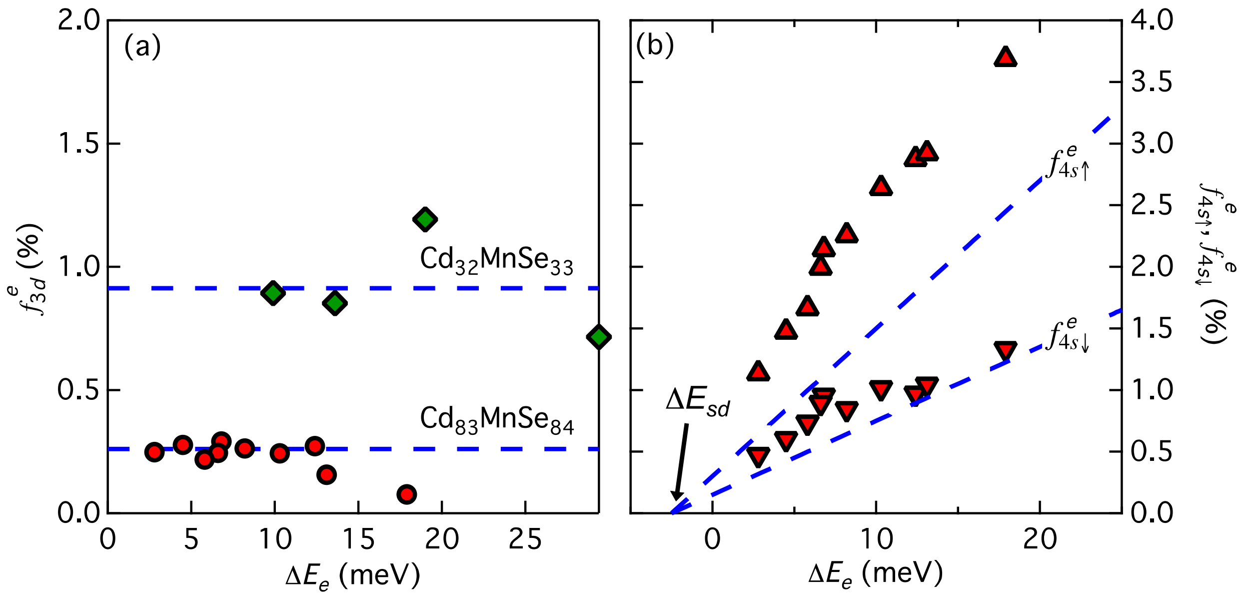

Figure 9. (a) Fractional Mn^{2+} 3*d* density in the CB electron orbital (f^{e}_{3d}) as a function of the Mn^{2+}-CB exchange splitting for $Cd_{83}MnSe_{84}$ QD (red circles) and $Cd_{32}MnSe_{33}$ QD (green diamonds). The blue dashed lines intercept the ordinate axis at 0.9 % ($Cd_{32}MnSe_{33}$ QD), and 0.3 % ($Cd_{83}MnSe_{84}$ QD). The surface positions are not included in this figure. **(b)** Fractional Mn^{2+} 4*s* density in both CB electron spin-orbitals of $Cd_{83}MnSe_{84}$ QD, corrected for the *s-d* exchange energy extracted from panel (a), ΔE_{sd} = -2.5 meV. The surface positions are not included in this figure.

Although not surpassing ΔE_{ss}, ΔE_{sd} is also not negligibly small. For the $Cd_{83}MnSe_{84}$ QDs, $\Delta E^{avg}_{sd} = -2.5$ meV and $\Delta E^{avg}_{ss} = +6.7$ meV, resulting in an overall splitting of $\Delta E_e = +4.2$ meV (Table 1). Kinetic *s-d* exchange is thus nearly 35% as effective as kinetic *s-s* exchange, and even ~20% as effective as kinetic *p-d* exchange (Table 2). At first glance, the increase of f^{e}_{3d} with decreasing QD diameter seen in Fig. 9(a) is suggestive of the increases in ΔE_{sd} with quantum confinement predicted from **k·p** theory.[36,37] From eq 16, the value of f^{e}_{3d} for $Cd_{32}MnSe_{33}$ QDs shown in Fig. 9(a) corresponds to $\Delta E^{avg}_{sd} = -5.2$ meV, which is indeed bigger than in the

$Cd_{83}MnSe_{84}$ QDs (−2.5 meV). However, eq 15 gives $\left|V_{sd}^{avg}\right|$ = 0.31 eV for the $Cd_{32}MnSe_{33}$ QD,[70] which is *smaller* than for the $Cd_{83}MnSe_{84}$ QD ($\left|V_{sd}^{avg}\right|$ = 0.41 eV, Table 2). We thus conclude that the increase in ΔE_{sd}^{avg} with decreasing QD diameter seen in Fig. 9(a) is *not* related to the influence of quantum confinement on the spatial part of the e_{CB}^{-} wavefunction, *i.e.*, is *not* from introduction of finite *k* vectors, but instead arises solely from the confinement-induced decrease in the energy spacing between CB edge and the empty $Mn^{2+}(3d)$ orbitals ($E_{3d\downarrow}–E_{CB}$ in eq 15). This energy gap is 0.6 eV for $Cd_{32}MnSe_{33}$ QDs, compared to 0.9 eV for $Cd_{83}MnSe_{84}$ QDs.[70] Quantum confinement can thus modulate ΔE_{sd} by tuning $E_{3d\downarrow}–E_{CB}$, but other bandgap engineering processes such as alloying will also lead to the same effect, as would shifting from Mn^{2+} to a more easily reduced dopant such as Co^{2+}.[47] Importantly, ΔE_{ss} also increases when the CB edge energy increases. It therefore does not appear possible to increase ΔE_{sd} without concomitantly increasing ΔE_{ss}, with the overall result that ΔE_e does not depend strongly on quantum confinement (see Fig. 4(b) and related text).[48] This conclusion contrasts sharply with the trends predicted from the $\mathbf{k\cdot p}$ approach[36,37] and claimed in some experimental reports,[36,37,41-45] but is consistent with the trends predicted from tight-binding calculations,[46] previous DFT calculations,[31,51] and other experimental results.[47]

In summary, these DFT and perturbation theory results predict that bulk-like kinetic *s-s* exchange dominates over kinetic *s-d* exchange in $Cd_{1-x}Mn_xSe$, even in QDs that are more strongly quantum confined than can be achieved experimentally. Although this analysis has focused on $Cd_{1-x}Mn_xSe$, the conclusions are readily generalized.

V. Discussion

The above analysis identifies the two orbital pathways that dominate all Mn^{2+}-carrier magnetic exchange coupling in DMSs, regardless of quantum confinement. Mn^{2+}-h_{VB}^{+} exchange is dominated by a *p-d* orbital pathway, and Mn^{2+}-e_{CB}^{-} exchange is dominated by an *s-s* orbital pathway. To illustrate these orbital interactions, Fig. 10 shows the e_{CB}^{-} and h_{VB}^{+} wavefunctions of Fig. 2 in the immediate vicinity of the Mn^{2+} ion. Substantial Mn^{2+} 3*d* character is evident in the h_{VB}^{+} wavefunction (Fig. 10(a)), reflecting the orbital pathway for kinetic *p-d* exchange responsible for $N_0\beta$. Contributions from the Cd^{2+} 4*d* orbitals are also evident, as detailed previously.[103] Figure 10(b) depicts this wavefunction schematically, showing a Mn^{2+} 3*d* orbital of t_2 symmetry (in the idealized T_d point symmetry of the cation site) hybridizing with a symmetry adapted linear combination (SALC) of Se^{2-} 5*p* orbitals also having t_2 symmetry, in an antibonding interaction. Regarding $N_0\alpha$, substantial Mn^{2+} 4*s* character is seen in the e_{CB}^{-} wavefunction (Fig. 10(c)). This wavefunction is illustrated schematically in Fig. 10(d), which shows the Mn^{2+} 4*s* atomic orbital of a_1 symmetry hybridizing with the a_1 SALC of Se^{2-} 5*p* orbitals in an antibonding interaction. The microscopic exchange processes described in the analysis section are thus readily visualized in the carrier wavefunctions themselves. We emphasize that the DFT calculations are not biased *a priori* toward any particular orbital pathway, in contrast with perturbation approaches.

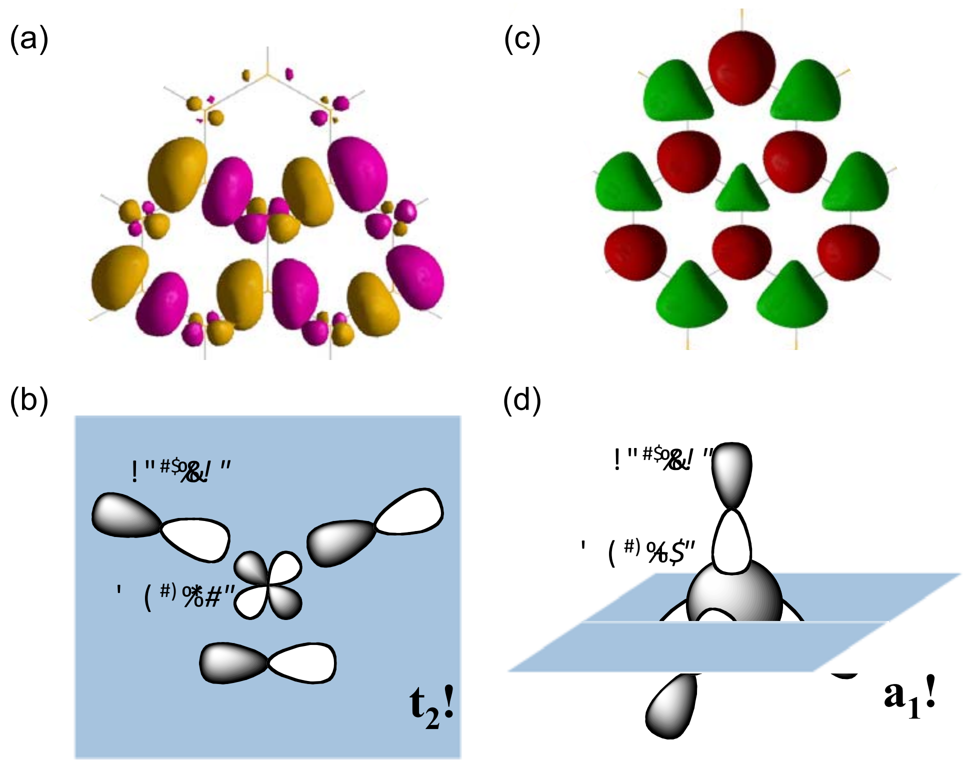

Figure 10. Dominant orbital pathways governing Mn^{2+}-carrier magnetic exchange in $Cd_{1-x}Mn_xSe$ QDs. **(a)** Close-up view of the h_{VB}^{+} wavefunction of Fig. 2 in the *c*-plane around the Mn^{2+} ion (center position). **(b)** Schematic depiction of the h_{VB}^{+} wavefunction shown in (a). The blue transparent plane is the *c*-plane containing the Mn^{2+} ion. The Mn^{2+} 3*d* orbital of t_2 symmetry hybridizes with the t_2 SALC of Se^{2-} 5*p* orbitals in an antibonding interaction. This interaction represents the orbital pathway for kinetic *p-d* exchange. **(c)** Close-up view of the e_{CB}^{-} wavefunction of Fig. 2 in the *c*-plane around the Mn^{2+} ion (center position). The

green lobes are s orbitals of Mn^{2+} (center) and the surrounding Cd^{2+} ions located in the same plane. The red lobes are the tops of neighboring Se^{2-} 5p orbitals. **(d)** Schematic depiction of the e^-_{CB} wavefunction shown in (c). The blue plane represents the c-plane containing the Mn^{2+} ion, rotated relative to (c) for clarity. The Mn^{2+} 4s orbital of a_1 symmetry hybridizes with the a_1 SALC of Se^{2-} 5p orbitals in an antibonding interaction. This interaction represents the orbital pathway for kinetic s-s exchange.

Importantly, even in the smallest QD studied here (d_{QD} = 1 nm, Fig. 4(b)), the Mn^{2+}- e^-_{CB} exchange interaction is ferromagnetic, which indicates that antiferromagnetic kinetic s-d exchange does not become more important than ferromagnetic kinetic s-s exchange even in such strongly confined DMSs. A threshold criterion for $N_0\alpha$ sign inversion was recently proposed on the basis of perturbation expressions and is summarized in eq 17.[48]

$$\Delta E_e < 0 \Leftrightarrow |V_{sd}| > \frac{|V_{ss}|}{2} \tag{17}$$

From Table 2, the DFT calculations yield $\left|V_{sd}^{avg}\right| \approx 0.2 \left|V_{ss}^{avg}\right|$ for the $Cd_{83}MnSe_{84}$ QD, failing to meet the criterion expressed by eq 17. Although changes in energy denominators may alter the specific threshold conditions relative to eq 17, the results above have shown that these transfer integrals are independent of QD diameter.

The balance between competing pathways is illustrated in Figure 11, which plots ΔE_{ss}, ΔE_{sd}, and ΔE_e vs the energy parameter $E_{4s\uparrow} - E_{CB}$ (a surrogate for confinement energy), calculated by eqs 13 and 15 using the DFT electronic structure as input. The three $Cd_{1-x}Mn_xSe$ QDs calculated by DFT are indicated as vertical lines. From this plot, ΔE_{ss} and ΔE_{sd} both increase as $E_{4s\uparrow} - E_{CB}$ decreases, with the result that ΔE_e remains relatively constant. Only when $E_{3d\downarrow} - E_{CB}$ approaches zero does ΔE_e begin to change significantly, but this resonance occurs at extremely small QD diameters (<1.5 nm). Of course, the nature of these curves relies heavily on the relative energies of the 3d(↓) and 4s(↑) levels. An important feature of the electronic structure of Mn^+ is that its $3d^54s^1$ configuration appears to be *lower* in energy than the $3d^6$ configuration in several experimentally documented cases.[99-101] If the level ordering observed in other crystals were maintained in DMSs, then $E_{4s\uparrow} - E_{CB}$ (eq 13) would be smaller than $E_{3d\downarrow} - E_{CB}$ (eq 15), and ΔE_e would actually *increase* with quantum confinement.[70] Despite the uncertain positions of the 3d(↓) and 4s(↑) levels, both scenarios predict a relatively small dependence of ΔE_e on quantum confinement until extremely small QD diameters.

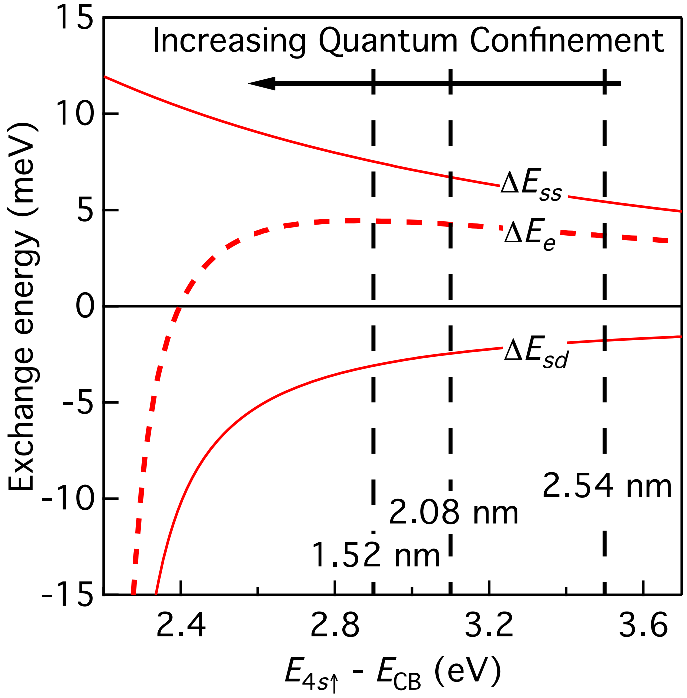

Figure 11. Quantum confinement effect on the total e^{-}_{CB}-Mn^{2+} magnetic exchange energy (ΔE_e) and on the kinetic *s*-*s* and *s*-*d* components (ΔE_{ss} and ΔE_{sd}). The energies of the Mn^{2+} 3*d* and 4*s* orbitals are pinned, and only the energy of the conduction band is allowed to change with confinement. The positions of the three $Cd_{1-x}Mn_xSe$ QDs calculated by DFT are given as vertical dashed lines. These calculations use $E_{4s\uparrow} - E_{3d\downarrow} = 2.2$ eV as calculated by DFT (Table 2).

VI. Conclusion

DFT calculations have been performed on $Cd_{1-x}Mn_xSe$ QDs to evaluate the microscopic Mn^{2+}-carrier exchange interactions that give rise to such defining characteristics of DMSs as the giant band-edge Zeeman splittings and carrier-mediated magnetic ordering. These calculations describe carrier wavefunctions and Mn^{2+}-carrier exchange energies without any of the usual assumptions such as mean-field or virtual-crystal approximations, or even the form of the effective exchange Hamiltonian. Atomistic and mean-field descriptions of DMS exchange interactions have been linked by analysis of the DFT electronic structure results using perturbation theory to predict Mn^{2+}-carrier exchange energies. Comparison of DFT results with properties predicted from perturbation theory shows good agreement between the two. This analysis has allowed the major orbital pathways mediating Mn^{2+}-carrier magnetic exchange to be evaluated individually, and the impact of quantum confinement to be assessed quantitatively. As established previously, the Mn^{2+}- h_{VB}^{+} interaction is dominated by *p-d* hybridization. The Mn^{2+}- e_{CB}^{-} interaction is shown to be dominated by spin-dependent *s-s* hybridization with a smaller opposing contribution from *s-d* hybridization. The sign of $N_0\alpha$ is not inverted in these strongly quantum confined $Cd_{1-x}Mn_xSe$ QDs relative to bulk $Cd_{1-x}Mn_xSe$. These results enrich our understanding of the microscopic origins of the unique physical properties of this class of materials.

Acknowledgments

Financial support from the U.S. National Science Foundation (Grant No. DMR-0906814 to D.R.G. and CHE-0844999 to X.L.) and additional support from Gaussian Inc. and the University of Washington Student Technology Fund are gratefully acknowledged.

References

[1] J. K. Furdyna, J. Appl. Phys. **64**, R29 (1988).
[2] J. K. Furdyna and J. Kossut eds., *Diluted Magnetic Semiconductors,* in *Semiconductors and Semimetals*, Vol. 25 (Academic Press, New York, 1988).
[3] J. Kossut and J. A. Gaj, Chapter 1 in *Introduction to the Physics of Diluted Magnetic Semiconductors*, edited by J. Kossut and J. A. Gaj (Springer-Verlag, Berlin, 2010), p. 1.
[4] R. Fiederling, M. Keim, G. Reuscher, W. Ossau, G. Schmidt, A. Waag, and L. W. Molenkamp, Nature **402**, 787 (1999).
[5] B. T. Jonker, Proc. IEEE **91**, 727 (2003).
[6] B. T. Jonker, Y. D. Park, B. R. Bennett, H. D. Cheong, G. Kioseoglou, and A. Petrou, Phys. Rev. B **62**, 8180 (2000).
[7] R. Beaulac, P. I. Archer, X. Liu, S. Lee, G. M. Salley, M. Dobrowolska, J. K. Furdyna, and D. R. Gamelin, Nano Lett. **8**, 1197 (2008).
[8] C. Drexler, V. V. Bel'kov, B. Ashkinadze, P. Olbrich, C. Zoth, V. Lechner, Y. V. Terent'ev, D. R. Yakovlev, G. Karczewski, T. Wojtowicz, D. Schuh, W. Wegscheider, and S. D. Ganichev, Appl. Phys. Lett. **97**, 182107 (2010).
[9] S. D. Ganichev, S. A. Tarasenko, V. V. Bel'kov, P. Olbrich, W. Eder, D. R. Yakovlev, V. Kolkovsky, W. Zaleszczyk, G. Karczewski, T. Wojtowicz, and D. Weiss, Phys. Rev. Lett. **102**, 156602 (2009).
[10] G. Bacher, Topics Appl. Phys. **90**, 147 (2003).
[11] R. Beaulac, L. Schneider, P. I. Archer, G. Bacher, and D. R. Gamelin, Science **325**, 973 (2009).
[12] A. K. Bhattacharjee, Phys. Rev. B **51**, 9912 (1995).
[13] A. K. Bhattacharjee and C. Benoit à la Guillaume, Phys. Rev. B **55**, 10613 (1997).
[14] R. Fiederling, D. R. Yakovlev, W. Ossau, G. Landwehr, I. A. Merkulov, K. V. Kavokin, T. Wojtowicz, M. Kutrowski, K. Grasza, G. Karczewski, and J. Kossut, Phys. Rev. B **58**, 4785 (1998).
[15] I. A. Merkulov, D. R. Yakovlev, K. V. Kavokin, G. Mackh, W. Ossau, A. Waag, and G. Landwehr, JETP Lett. **62**, 335 (1995).

[16] P. A. Wolff, in *Semiconductors and Semimetals*, edited by J. K. Furdyna and J. Kossut (Academic Press, New York, 1988), Vol. 25, p. 413.
[17] T. Dietl, H. Ohno, F. Matsukura, J. Cibert, and D. Ferrand, Science **287**, 1019 (2000).
[18] K. R. Kittilstved, D. A. Schwartz, A. C. Tuan, S. M. Heald, S. A. Chambers, and D. R. Gamelin, Phys. Rev. Lett. **97**, 037203 (2006).
[19] J. König and A. H. MacDonald, Phys. Rev. Lett. **91**, 077202 (2003).
[20] D. A. Schwartz and D. R. Gamelin, Adv. Mater. **16**, 2115 (2004).
[21] R. Beaulac, P. I. Archer, S. T. Ochsenbein, and D. R. Gamelin, Adv. Funct. Mater. **18**, 3873 (2008).
[22] R. Beaulac, S. T. Ochsenbein, and D. R. Gamelin, Chapter 11 in *Semiconductor Quantum Dots*, edited by V. I. Klimov (CRC Press, 2010), p. 397.
[23] F. Henneberger and J. Puls, Chapter 5 in *Introduction to the Physics of Diluted Magnetic Semiconductors*, edited by J. Kossut and J. A. Gaj (Springer-Verlag, Berlin, 2010), p. 161.
[24] D. Loss and D. P. DiVincenzo, Phys. Rev. A **57**, 120 (1998).
[25] I. Žutić, J. Fabian, and S. Das Sarma, Rev. Mod. Phys. **76**, 323 (2004).
[26] J. Fernández-Rossier and R. Aguado, Phys. Stat. Sol. (c) **3**, 3734 (2006).
[27] R. M. Abolfath, A. G. Petukhov, and I. Žutić, Phys. Rev. Lett. **101**, 207202 (2008).
[28] R. Oszwałdowski, I. Žutić, and A. G. Petukhov, Phys. Rev. Lett. **106**, 177201 (2011).
[29] A. O. Govorov, Phys. Rev. B **72**, 075358 (2005).
[30] F. Qu and P. Hawrylak, Phys. Rev. Lett. **95**, 217206 (2005).
[31] S. T. Ochsenbein, Y. Feng, K. M. Whitaker, E. Badaeva, W. K. Liu, X. Li, and D. R. Gamelin, Nature Nanotechnol. **4**, 681 (2009).
[32] Y. G. Semenov and B. D. Shanina, Phys. Stat. Sol. (b) **104**, 631 (1981).
[33] A. K. Bhattacharjee, G. Fishman, and B. Coqblin, Physica B **117-118**, 449 (1983).
[34] B. E. Larson, K. C. Hass, H. Ehrenreich, and A. E. Carlsson, Phys. Rev. B **37**, 4137 (1988).
[35] P. Kacman, Semicond. Sci. Technol. **16**, R25 (2001).
[36] I. A. Merkulov and A. V. Rodina, Chapter 3 in *Introduction to the Physics of Diluted Magnetic Semiconductors*, edited by J. Kossut and J. A. Gaj (Springer-Verlag, Berlin, 2010), p. 65.
[37] I. A. Merkulov, D. R. Yakovlev, A. Keller, W. Ossau, J. Geurts, A. Waag, G. Landwehr, G. Karczewski, T. Wojtowicz, and J. Kossut, Phys. Rev. Lett. **83**, 1431 (1999).
[38] A. K. Bhattacharjee, Phys. Rev. B **58**, 15660 (1998).
[39] A. K. Bhattacharjee and J. Pérez-Conde, Phys. Stat. Sol. (b) **241**, 672 (2004).
[40] G. M. Dalpian and S.-H. Wei, Phys. Rev. B **73**, 245204 (2006).
[41] D. A. Bussian, S. A. Crooker, M. Yin, M. Brynda, Al. L. Efros, and V. I. Klimov, Nature Mater. **8**, 35 (2009).
[42] J. H. Yu, X. Liu, K. E. Kweon, J. Joo, J. Park, K.-T. Ko, D. W. Lee, S. Shen, K. Tivakornsasithorn, J. S. Son, J.-H. Park, Y.-W. Kim, G. S. Hwang, M. Dobrowolska, J. K. Furdyna, and T. Hyeon, Nature Mater. **9**, 47 (2010).
[43] R. C. Myers, M. Poggio, N. P. Stern, A. C. Gossard, and D. D. Awschalom, Phys. Rev. Lett. **95**, 017204 (2005).
[44] N. P. Stern, R. C. Myers, M. Poggio, A. C. Gossard, and D. D. Awschalom, Phys. Rev. B **75**, 045329 (2007).
[45] I. I. Reshina and S. V. Ivanov, Semicond. **45**, 215 (2011).
[46] A. K. Bhattacharjee and J. Pérez-Conde, in *Proceedings of the 25th International Conference on the Physics of Semiconductors*, edited by N. Miura and T. Ando (Springer-Verlag, Berlin, 2000), p. 242.
[47] V. A. Vlaskin, R. Beaulac, and D. R. Gamelin, Nano Lett. **9**, 4376 (2009).
[48] R. Beaulac and D. R. Gamelin, Phys. Rev. B **82**, 224401 (2010).
[49] E. Badaeva, Y. Feng, D. R. Gamelin, and X. Li, New J. Phys. **10**, 055013 (2008).
[50] E. Badaeva, C. M. Isborn, Y. Feng, S. T. Ochsenbein, D. R. Gamelin, and X. Li, J. Phys. Chem. C **113**, 8710 (2009).
[51] C. Echeverría-Arrondo, J. Pérez-Conde, and A. Ayuela, Phys. Rev. B **79**, 155319 (2009).
[52] C. Echeverría-Arrondo, J. Pérez-Conde, and A. Ayuela, Phys. Rev. B **82**, 205419 (2010).

[53] Y. Feng, E. Badaeva, D. R. Gamelin, and X. Li, J. Phys. Chem. Lett. **1**, 1927 (2010).
[54] S. Ghosh, B. Sanyal, and G. P. Das, Appl. Phys. Lett. **96**, 052506 (2010).
[55] N. S. Norberg, G. M. Dalpian, J. R. Chelikowsky, and D. R. Gamelin, Nano Lett. **6**, 2887 (2006).
[56] Y.-N. Xu and W. Y. Ching, Phys. Rev. B **48**, 4335 (1993).
[57] C. de Mello Donegá, S. G. Hickey, S. F. Wuister, D. Vanmaekelbergh, and A. Meijerink, J. Phys. Chem. B **107**, 489 (2003).
[58] C. B. Murray, D. J. Norris, and M. G. Bawendi, J. Am. Chem. Soc. **115**, 8706 (1993).
[59] D. V. Talapin, A. L. Rogach, A. Kornowski, M. Haase, and H. Weller, Nano Lett. **1**, 207 (2001).
[60] A. I. Ekimov, F. Hache, M. C. Schanne-Klein, D. Ricard, C. Flytzanis, I. A. Kudryavtsev, T. V. Yazeva, A. V. Rodina, and Al. L. Efros, J. Opt. Soc. Am. B **10**, 100 (1993).
[61] L.-W. Wang and J. Li, Phys. Rev. B **69**, 153302 (2004).
[62] X. Huang, E. Lindgren, and J. R. Chelikowsky, Phys. Rev. B **71**, 165328 (2005).
[63] M. J. Frisch, G. W. Trucks, H. B. Schlegel, G. E. Scuseria, M. A. Robb, J. R. Cheeseman, G. Scalmani, V. Barone, B. Mennucci, G. A. Petersson, H. Nakatsuji, M. Caricato, X. Li, H. P. Hratchian, A. F. Izmaylov, J. Bloino, G. Zheng, J. L. Sonnenberg, M. Hada, M. Ehara, K. Toyota, R. Fukuda, J. Hasegawa, M. Ishida, T. Nakajima, Y. Honda, O. Kitao, H. Nakai, T. Vreven, J. Montgomery, J. A., J. E. Peralta, F. Ogliaro, M. Bearpark, J. J. Heyd, E. Brothers, K. N. Kudin, V. N. Staroverov, R. Kobayashi, J. Normand, K. Raghavachari, A. Rendell, J. C. Burant, S. S. Iyengar, J. Tomasi, M. Cossi, N. Rega, N. J. Millam, M. Klene, J. E. Knox, J. B. Cross, V. Bakken, C. Adamo, J. Jaramillo, R. Gomperts, R. E. Stratmann, O. Yazyev, A. J. Austin, R. Cammi, C. Pomelli, J. W. Ochterski, R. L. Martin, K. Morokuma, V. G. Zakrzewski, G. A. Voth, P. Salvador, J. J. Dannenberg, S. Dapprich, A. D. Daniels, Ö. Farkas, J. B. Foresman, J. V. Ortiz, J. Cioslowski, and D. J. Fox, (Gaussian, Inc., Wallingford, CT, 2011).
[64] J. P. Perdew, K. Burke, and M. Ernzerhof, Phys. Rev. Lett. **77**, 3865 (1996).
[65] J. P. Perdew, K. Burke, and M. Ernzerhof, Phys. Rev. Lett. **78**, 1396 (1997).
[66] C. Adamo and V. Barone, J. Chem. Phys. **110**, 6158 (1999).
[67] P. J. Hay and W. R. Wadt, J. Chem. Phys. **82**, 270 (1985).
[68] P. J. Hay and W. R. Wadt, J. Chem. Phys. **82**, 299 (1985).
[69] W. R. Wadt and P. J. Hay, J. Chem. Phys. **82**, 284 (1985).
[70] See EPAPS Document No. [number will be inserted by AIP] for additional data on the $Cd_{32}MnSe_{33}$ and $Cd_{152}MnSe_{153}$ QDs and for the modified pseudopotentials used in Fig. 8. For more information on EPAPS, see http://www.aip.org/pubservs/epaps.html.
[71] M. G. Bawendi, M. L. Steigerwald, and L. E. Brus, Annu. Rev. Phys. Chem. **41**, 477 (1990).
[72] A. Kasuya, R. Sivamohan, Y. A. Barnakov, I. M. Dmitruk, T. Nirasawa, V. R. Romanyuk, V. Kumar, S. V. Mamykin, K. Tohji, B. Jeyadevan, K. Shinoda, T. Kudo, O. Terasaki, Z. Liu, R. V. Belosludov, V. Sundararajan, and Y. Kawazoe, Nature Mater. **3**, 99 (2004).
[73] R. W. Meulenberg, J. R. I. Lee, A. Wolcott, J. Z. Zhang, L. J. Terminello, and T. van Buuren, ACS Nano **3**, 325 (2009).
[74] E. Runge and E. K. U. Gross, Phys. Rev. Lett. **52**, 997 (1984).
[75] L. Hedin, Phys. Rev. **139**, A796 (1965).
[76] O. Matumura, J. Phys. Soc. Jpn. **14**, 108 (1959).
[77] A. Franciosi, S. Chang, C. Caprile, R. Reifenberger, and U. Debska, J. Vac. Sci. Technol. A **3**, 926 (1985).
[78] B. A. Orlowski, K. Kopalko, and W. Chab, Solid State Commun. **50**, 749 (1984).
[79] M. Taniguchi, M. Fujimori, M. Fujisawa, T. Mori, I. Souma, and Y. Oka, Solid State Commun. **62**, 431 (1987).
[80] P. Guyot-Sionnest, Microchim. Acta **160**, 309 (2008).
[81] W. K. Liu, K. M. Whitaker, K. R. Kittilstved, and D. R. Gamelin, J. Am. Chem. Soc. **128**, 3910 (2006).
[82] L. Besombes, Y. Léger, L. Maingault, and H. Mariette, J. Appl. Phys. **101**, 081713 (2007).
[83] S. A. Blanton, R. L. Leheny, M. A. Hines, and P. Guyot-Sionnest, Phys. Rev. Lett. **79**, 865 (1997).
[84] M. Shim and P. Guyot-Sionnest, J. Chem. Phys. **111**, 6955 (1999).

[85] J. Kossut and J. A. Gaj eds., *Introduction to the Physics of Diluted Magnetic Semiconductors* (Springer-Verlag, Berlin, 2010).

[86] Experimentally, the Mn^{2+} magnetization vector opposes the direction of the external magnetic field, and the quantity $\langle S_z \rangle$ is thus often taken to saturate at negative values, *i.e.*, $\langle S_z \rangle = -2.5$. The convention in this study then corresponds experimentally to the application of a saturating negative magnetic field oriented along the C_3-axis of the QDs.

[87] M. Arciszewska and M. Nawrocki, J. Phys. Chem. Solids **47**, 309 (1986).

[88] D. Scalbert, M. Nawrocki, C. Benoit à la Guillaume, and J. Cernogora, Phys. Rev. B **33**, 4418 (1986).

[89] X.-W. Zhang, W.-J. Fan, K. Chang, S.-S. Li, and J.-B. Xia, Appl. Phys. Lett. **91**, 113108 (2007).

[90] O. Madelung, *Semiconductors Data Handbook* (Springer, Berlin, 2004).

[91] Inclusion of hole degeneracy in the carrier distribution function (*i.e.*, including second-order spherical Bessel function components, see *e.g.* Al. L. Efros, M. Rosen, M. Kuno, M. Nirmal, D. J. Norris, and M. Bawendi, Phys. Rev. B, **54**, 4843 (1996)) does not lead to a qualitatively different curvature than that given by eq 6.

[92] P. S. Dorozhkin, A. V. Chernenko, V. D. Kulakovskii, A. S. Brichkin, A. A. Maksimov, H. Schoemig, G. Bacher, A. Forchel, S. Lee, M. Dobrowolska, and J. K. Furdyna, Phys. Rev. B **68**, 195313 (2003).

[93] D. U. Bartholomew, E.-K. Suh, S. Rodriguez, A. K. Ramdas, and R. L. Aggarwal, Solid State Commun. **62**, 235 (1987).

[94] B. E. Larson, K. C. Hass, and R. L. Aggarwal, Phys. Rev. B **33**, 1789 (1986).

[95] P. W. Anderson, in *Magnetism*, edited by G. T. Rado and H. Suhl (Academic Press, New York, 1963), Vol. 1, p. 25.

[96] P. W. Anderson, Solid State Phys. **14**, 99 (1963).

[97] J. B. Goodenough, *Magnetism and the Chemical Bond* (John Wiley & Sons, New York, 1963).

[98] H. Weihe and H. U. Güdel, Inorg. Chem. **36**, 3632 (1997).

[99] M. Ikeya and N. Itoh, J. Phys. Chem. Solids **32**, 2569 (1971).

[100] V. M. Orera, P. J. Alonso, R. Cases, and R. Alcala, Radiat. Eff. **83**, 213 (1984).

[101] C. Corliss and J. Sugar, J. Phys. Chem. Ref. Data **6**, 1253 (1977).

[102] R. S. Mulliken, J. Chem. Phys. **23**, 2343 (1955).

[103] S.-H. Wei and A. Zunger, Phys. Rev. B **37**, 8958 (1988).